Xenon plasma-FIB micromachined cavity-based fiber sensors for refractive index, temperature and chemical sensing

Khan, Inam; Machavaram, V. R.; Ma, T.; Feather, L.; Gao, X.; Wu, Jing; Chiu, Yu Lung; Fernando, Gerard F.

DOI:
10.1364/OSAC.414955

Research Article Vol. 4, No. 6 / 15 June 2021 / OSA Continuum 1736

Xenon plasma-FIB micromachined cavity-based fiber sensors for refractive index, temperature and chemical sensing

INAM KHAN,[1] V. R. MACHAVARAM,[1,2,*] T. MA,[1] L. FEATHER,[1] X. GAO,[1] JING WU,[1] YU LUNG CHIU,[1] AND GERARD F. FERNANDO[1]

[1] *School of Metallurgy and Materials, University of Birmingham, Edgbaston, Birmingham, B15 2TT, UK*
[2] *Department of Physics, Dr APJ Abdul Kalam Campus, RGUKT, Ongole-523001, India*
[*] *machavvr@aol.co.uk*

Abstract: Xenon plasma-FIB micromachining has been used for relatively rapid (10-20 minutes) production of intrinsic Fabry-Perot cavities in fused silica single and multimode fibers without any post-processing. Infiltration of organic solvents into the cavity produced in the proximity of cleaved-end of a single mode fiber has enabled refractive index sensing with a sensitivity of ~-65 dB/riu in the range 1.31-1.37. The influence of cavity wall-angle and cleave imperfections on the performance of the sensor have been discussed. Theoretical interpretation shows that the index sensitivity and measurement range can be tailored via the length of the cavity and its distance from the cleaved-end. The same sensor when heated up to 900 °C has shown a wavelength-temperature sensitivity of 8.1 pm/°C and 8.7 pm/°C during the first and second heating cycles respectively owing to the irreversible effects of dopant-diffusion. Multimode fiber cavity has enabled chemical sensing via NIR-absorption spectroscopy of an epoxy resin, amine-based hardener and its affinity for atmospheric moisture, offering scope for remote chemical process monitoring of engineering materials and structures.

1. Introduction

Intrinsic fiber Fabry-Perot sensors based on air cavities are fabricated largely by means of 157 nm-excimer [1,2] and femto-second laser micromachining [3,4]; chemical etching of cleaved fibers [5–7]; and focussed ion beam (FIB) milling [8,9]. The salient features of these interferometric sensors are that their diameter is virtually the same as that of the fiber and devoid of foreign material as compared to extrinsic fiber Fabry-Perot interferometer [10] where the fibers are housed inside a silica capillary of larger diameter. Hence, they offer miniaturisation and new functionality by the virtue of their design. The natural chemical inertness and durability of fused silica fibers at high temperatures and high pressures render these sensors fit for use in harsh environments. Laser micromachining offers scope for rapid production of through-diameter and cleaved-end-on Fabry-Perot (FP) cavities in silica fibers. However, as governed by the pulsed laser-material interactions, the topography of high-aspect ratio microcavities in fused silica is often accompanied by one or more of the unwanted effects to a varying degree in the form of surface swelling and rugged topography, ablation debris, microcracking and cavity wall-tapering [11,12]. These collateral effects can be detrimental to the optical performance and the mechanical integrity of the fiber sensor. Therefore, controlling measures during production or post-production treatments are usually employed. For example, the use of KOH-assisted ultrafast laser micromachining [13] of fused silica enabled controlled production of channels to a depth of several millimetres. HF-treatment of F_2-laser micromachined [14] fused silica was used to determine the ablation-induced stresses in the surface layer and to estimate the threshold energy

#414955 https://doi.org/10.1364/OSAC.414955
Journal © 2021 Received 16 Nov 2020; revised 17 Mar 2021; accepted 30 Mar 2021; published 19 May 2021

OSA CONTINUUM

density for the onset of microcracks. Bellouard [15] used HF-etching to reduce the ultrafast laser-induced density of topographical surface peaks that act as stress concentrators after the production of micro-flexures in fused silica.

On the other-hand, liquid Gallium-based FIB enables micromachining of relatively more complex geometries with relatively less collateral damage and also enable better depth resolution and process control [16,17]. FIB micromachining is used extensively for 3D-micro and nano-structuring of materials in semiconductor industry, transmission electron microscopy and micro-electromechanical systems. Li *et al*. [18] used FIB to micromachine a slot close to the cleaved-end of the fiber in two steps where the controlled thickness of the gold coating enabled production of a semi-transparent input etalon and a mirror-coated reflector etalon to act as a 2-beam interferometer for refractive index sensing of liquids with in the cavity. Nguyen *et al*. [19] reported on an FIB-micromachined cavity near the cleaved-end of the fiber to form a 3-beam interferometer to detect the salinity of water filling the cavity. The wavelength-salinity sensitivity at constant temperature and wavelength-temperature sensitivity at constant salinity for different fringes were found to be different as governed by the relative phase changes of the combined Fabry-Perot cavities. This enabled simultaneous measurement of salinity and temperature via the cross-sensitivity matrix. Other techniques such as splicing a hollow fiber section to two fibers [20–22]; controlled production of micro-air-bubble at the tip of a fiber [23]; and air-entrapment between the fiber and a molten metal microsphere [24] have been also demonstrated.

Majority of the reports on FP cavity sensors are based on 2-beam interference where the change in optical path difference is usually measured via the change in cavity length [4] or shift in wavelength of a fringe [25,26] depending on the magnitude of change in measurand. Sensors based on 3-beam fiber interferometers are generally based on the measurement of fringe contrast [27,28] of the sealed Fabry-Perot air-cavity as influenced by the Fresnel reflectivity at the distal cleaved-end of the fiber in contact with the medium; optical path difference [22] and on the time taken to traverse the optical path difference [29] as a result of infiltration of medium into the cavity. The production of these sensors [22,28–29] requires skilful manual operations such as precision cleaving of fibers to short lengths; controlled etching and fusion-splicing of coated-fiber ends and delicate handling.

Majority of the reports on FIB micromachined fiber sensors were based on Ga^+-FIB. In the current paper, we demonstrate Xe^+-FIB micromachining of cavities in fused silica optical fibers. The chemical inertness, large atomic mass of xenon plasma in conjunction with high beam current enables large-volume micromachining with minimal surface damage in reduced processing time without contamination as compared to the conventional Ga^+-FIB-based micromachining [30,31]. For example, Zhong *et al.* [32] reported that Xe^+-FIB-milled 'Al' alloy TEM samples were cleaner without 'Xe' enrichments at grain boundaries; low surface artefacts due to redeposition; and large areas transparent to electrons were produced as compared to Ga^+-FIB milling. The use of Xe^+-FIB enabled direct fabrication of atom probe tomography needles onto flat samples of Ti-6Al-4V alloy, bypassing the ion damage, implantation and reactivity issues accompanied by Ga^+-FIB milling-based production [33]. Therefore, this work also demonstrates the potential of Xe^+-FIB for producing Fabry-Perot microcavities in fused silica optical fibers. The influence of cavity geometry on fringe visibility was studied. A rectangular cavity was micromachined in the proximity of the cleaved-end with the rationale of producing a simple single-ended sensor fit for refractive index and temperature sensing. Firstly, this sensor was deployed to measure the refractive index of organic solvents. Subsequently, the response of the sensor up to ~900 °C was studied during two heating cycles. Fast Fourier transform-based signal processing was carried out. The influence of cavity wall-tapering on direct determination of refractive index via traverse-time estimation was analysed. A cavity produced in fused silica multimode fiber was used as a micro-spectroscopic cell to obtain the absorption spectrum of a thermosetting resin and

OSA CONTINUUM

amine-based hardener via FTIR spectroscopy. The affinity of amine for atmospheric moisture was also sensed through absorption spectrum.

2. Materials and methods

2.1. Sensor production

Fused silica optical fiber (SMF 28) was micromachined by means of an inductively coupled Xenon (Xe^+) plasma focussed ion beam (FIE FIB/SEM Helios G4 CX system) workstation. The stripped and cleaned fiber was sputter-coated with gold/palladium alloy at 25 mA current for 3 minutes prior to milling. This was done to avoid charging of sample surface and drifting of FIB. The coated fiber was grounded by means of a carbon adhesive tab stuck to the mounting metal stub. At an accelerating voltage of 30 kV, a beam current of 1 µA was used to machine a rectangular area (~110 µm x 80 µm) centred over the cylindrical surface of the fiber. The excision was carried out through-thickness of the fiber for about 20 minutes to produce a rectangular hole whose length was parallel to the fiber axis. The microstructure was located at a distance of few tens of micrometres from the cleaved-end of the fiber. The remainder of the optical fiber was coiled, secured, and suspended on the side of the aluminium stub. After micromachining, the cleaved-end was positioned at the proximity of the electrodes of a BFS-60 manual fiber-optic fusion splicer (BIT, UK) with the aid of integral microscope and the coating was removed by means of low-current electric arcs generated for short duration. Circular through-thickness cavities were also produced in SMF 28 fibers. With reference to the multi-mode optical fibers (FG105LCA, Thorlabs), the FIB was operated using a similar set of conditions to that mentioned previously. However, in this instance, the centre potion of a length of optical fiber was stripped, cleaned and sputter-coated as mentioned previously. The end-sections of the multi-mode optical fiber were coiled, secured and suspended on the side of the aluminium stubs.

The optical response of the cavity in fiber was studied using a sweep-laser source-based FBG interrogator (sm130, Micron Optics Inc.) which operates in the wavelength range of 1510-1590 nm and enables fast dynamic measurements at a sampling rate of 1000 Hz. It offers a wavelength repeatability of 1-0.05 pm with 1000 averages. The wavelength stability was typically 2-5 pm. The FIB-micromachined sensor was fusion-spliced to an SMF 28 fiber pigtailed patch cable with FC/APC termination plugged into the front panel FC/APC optical connector of the interrogator.

2.2. Refractive index sensing

Analytical reagent grade organic solvents (methanol, acetonitrile, ethanol, acetone, isopropanol) supplied by Sigma-Aldrich were taken into 20 ml glass vials at laboratory ambient at 25 °C. Solvent temperature was measured using a k-type thermocouple. The solvent temperature during measurements was 25 ± 1.5 °C. The cleaved-end of the fiber including the cavity was fully immersed for solvent infiltration and the resulting signals were obtained for each solvent after 2-3 minutes of immersion. Upon withdrawal from a solvent-filled vial, the solvent was allowed to evaporate fully at laboratory ambient and the signal of air-filled cavity was retrieved prior to next immersion. It was observed that the evaporation of solvent from the cavity which was open at both ends occurred over a period of few seconds, typically <10 s. However, the sensor was left at ambient for 3-4 minutes prior to immersion in a different solvent. Immersion in each solvent was repeated three times to see the signal repeatability.

2.3. Temperature sensing

The sensor was bonded using a ceramic adhesive over the stripped length of the fiber to the flat surface of a high temperature ceramic substrate, which constituted fused silica as the major component (80-85 wt%) in conjunction with alumina and zircon, about 4 cm away from the

OSA CONTINUUM

sensing end of the fiber. The section of the fiber length towards the sensing end was devoid of bends. The mounted sensor was placed at the centre of a tube furnace. The temperature was ramped to different set isothermal temperatures with a variation of about ±2 °C during the dwell period of about 15-20 minutes and the corresponding optical signals were recorded. An R-type thermocouple in conjunction with PicoLog data logger was used to infer the temperature in the proximity of the sensing-end of the fiber.

2.4. Chemical sensing

FIB-micromachined cavity of dimensions ~129 µm x 67 µm through the diameter of a multimode fiber (FG105LCA, Thorlabs) was used for the infiltration of liquid medium whose absorption spectrum was of interest. Here we used a thermoset resin system, epoxy resin (Araldite LY3505) and amine-based hardener (XB3403). The sensor was laid straight along the length of a glass slide and bonded at two points away from the cavity using a UV-curable adhesive. This glass slide was placed in a Petri dish and the resin was introduced until the sensor was fully immersed. An external white light source (WLS100, Bentham Instruments) was used at the input end of the fiber and the transmitted light through the cavity was measured using an FTIR detector (Bruker MATRIX -F DUPLEX FT-NIR spectrometer, Bruker Optics Ltd., UK).

3. Operating principles

Schematic of a Fabry-Perot cavity in the proximity of the cleaved-end of an optical fiber is shown in Fig. 1. The spectral interference of the Fresnel reflection 1, 2 and 3 can be expressed as:

$$I = |E|^2 = I_1 + I_2 + I_3 - 2\sqrt{I_1 I_2}\cos\phi_1 - 2\sqrt{I_2 I_3}\cos\phi_2 + 2\sqrt{I_1 I_3}\cos(\phi_1 + \phi_2) \quad (1)$$

$$I_1 = I_0 A^2 = E_0^2 A^2;\ I_2 = I_0 B^2;\ I_3 = I_0 C^2 \quad (2)$$

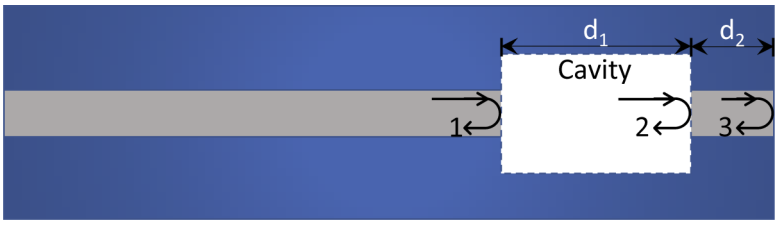

Fig. 1. Schematic sensor design illustrating the Fresnel reflections at the boundaries separating the core/air.

A, B and C are constants determined by the Fresnel reflectivity at the boundaries and round-trip insertion losses [34] as the light passes through d_1 and d_2. E_0 is the input field amplitude; ϕ_1 and ϕ_2 are the optical phases accumulated due to $2d_1$ and $2d_2$ respectively. n_f is the effective refractive index of the core while n_m is the refractive index of the medium filling the cavity.

Therefore, the spectral modulation is determined by the sum of three cosine terms. Let ϕ_{12} be the total round-trip phase change due to d_1 and d_2.

$$\phi_1 = \frac{2\pi}{\lambda}.n_m.2d_1;\ \phi_2 = \frac{2\pi}{\lambda}.n_f.2d_2;\ \phi_{12} = \phi_1 + \phi_2 \quad (3)$$

Upon differentiating ϕ_{12} in Eq. (3) and some juggling

$$\frac{\Delta\phi_{12}}{\phi_{12}} = \frac{-\Delta\lambda}{\lambda} + \frac{\phi_1}{\phi_{12}}\left(\frac{\Delta n_m}{n_m} + \frac{\Delta d_1}{d_1}\right) + \frac{\phi_2}{\phi_{12}}\left(\frac{\Delta n_f}{n_f} + \frac{\Delta d_2}{d_2}\right) \quad (4)$$

OSA CONTINUUM

$$\Delta\phi_{12} = \Delta\phi_1 + \Delta\phi_2 \tag{5}$$

If $\Delta\phi_2$=0 and $\Delta\phi_1$<2π then ($\Delta\phi_{12}/\phi_{12}$) <<1 and can be neglected. Hence the measurand-induced shift in the wavelength corresponding to a specified peak or valley of a fringe can be determined without order ambiguity. Then Eq. (4) gets transformed as:

$$\frac{\Delta\lambda}{\lambda} = \frac{\phi_1}{\phi_{12}}\left(\frac{\Delta n_m}{n_m} + \frac{\Delta d_1}{d_1}\right) \tag{6}$$

As $\Delta\phi_2$=0 and $\Delta\phi_{12}$=$\Delta\phi_1$, if the phase change $\Delta\phi_1$=2nπ, n is an integer, then

$$\Delta\phi_1 = \frac{4\pi}{\lambda}.d_1.\Delta n_m \tag{7}$$

$$\Delta n_m = \frac{n\lambda}{2d_1} \tag{8}$$

The wavelength-refractive index sensitivity when Δd_1~0 in Eq. (6) and the refractive index range for $\Delta\phi_1$=2π according (8) are estimated and plotted in Fig. 2 for different initial values of d_1. Here, the sensing-end of the fiber is assumed to be initially immersed in a liquid of refractive index 1.3174 at 1550 nm and d_2=25 μm. It is readily apparent that larger d_1 offers higher sensitivity at the expense of index range. However, the insertion loss will also increase with cavity length d_1. It can also be inferred from Eqs. (6) and (8) that if d_2 is reduced keeping d_1 constant, the sensitivity increases with d_1/d_2. When $d_2 \rightarrow 0$, the sense of third reflection disappears as $\phi_2 \rightarrow 0$ and the relative change in refractive index equals the relative shift in wavelength. Here the index range remains unchanged according to Eq. (8). A detailed mathematical theory of 3-beam fiber interferometer can be found in [27].

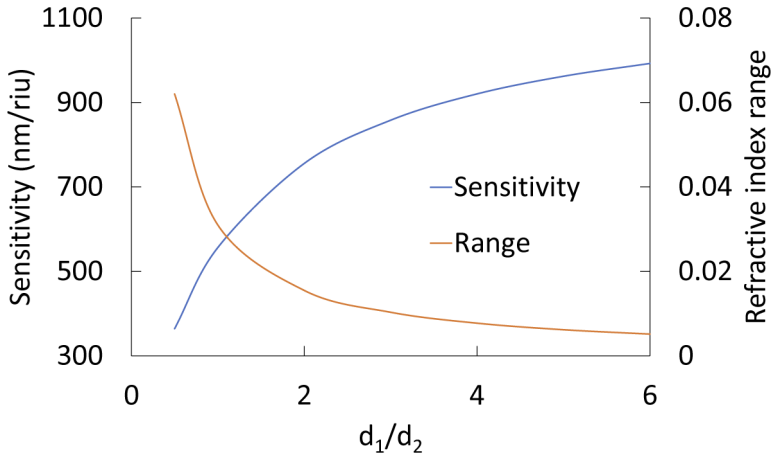

Fig. 2. Plot showing the influence of d_1(12.5 μm to 150 μm) and d_2=25 μm on sensitivity and the index range at 1550 nm for $\Delta\phi_1$=2π.

If Δn_m results in $\Delta\phi_1 \geq 2\pi$, then FFT-based analysis of compound spectrum can impart the influence of the measurand on the frequency components present in the spectrum [28]. The frequency components due to ϕ_1, ϕ_2 and ϕ_{12} can be obtained via a fast Fourier transform of the interference signal generated using Eq. (1) for d_1=125 μm and d_2=25 μm. Here the values of refractive index of the liquid medium in which the sensing end of the fiber is assumed to be immersed with the medium infiltrating the cavity, correspond to 2π phase increments from ϕ_1 to ϕ_1+10π at 1550 nm as determined using Eqs. (7) and (8). The sampling interval of wavelength was ~4 pm in the wavelength range of 1510-1590 nm with 19776 points followed by

OSA CONTINUUM

zero-buffering till 32768 points. Subsequently, the FFT output was interpolated with a sample spacing of 0.1 using cubic spline fit to enable peak location more accurately. Figure 3 shows the FFTs of compound spectra for different values of n_m. Peaks 1 and 2 correspond to the frequency components due to ϕ_2 and ϕ_1 respectively. Peak 3 corresponds to ϕ_{12} or the longest optical path $2(n_m d_1 + n_f d_2)$. The sensitivity of peak intensities to refractive index is shown in Fig. 4. The peak intensities decrease with increasing refractive index in general, but at different rates as governed by the optical paths through d_1 and d_2 and the associated insertion losses. Peak 3 shows greatest sensitivity to refractive index as the reflection 3 is determined by reflectivities at three boundaries separating n_m and the fiber. The light coupled into the section d_2 from the liquid-filled section d_1 and the subsequent Fresnel reflection at the distal end of the sensor are considered lossless with in the section d_2 as they are assumed to be guided by the fiber. The coupled part of reflection 2 into the fiber was calculated as follows: Firstly, the light coupled into section d_2 is calculated using the longitudinal gap-induced insertion loss equations in [34] in conjunction with the reflection losses. This is followed by the determination of Fresnel reflected part (reflection 2 in Fig. 1) of the uncoupled light. Here the light incident on the cladding is also considered as uncoupled light. The fraction of reflection 2 coupled into the fiber is equivalent to the light coupled into a receiving fiber from a light emanating fiber at a longitudinal separation of $2d_1$ occupied by n_m. Here the light emanated from the fiber is equal to the magnitude of reflection 2. The infiltrated medium is considered non-absorbing with in the wavelength range. Accordingly, the calculations yield 0.0316% and 0.0987% of input light as the coupled fractions of 2^{nd} and 3^{rd} Fresnel reflections respectively for n_m=1.3174. The first peak magnitude is determined by reflections 2 and 3 whilst the optical path length corresponding to d_2 is insensitive to refractive index changes of the medium at laboratory ambient temperature in which the sensing end is immersed. In this method, a linear response (Fig. 4) can be expected over a relatively wide range as compared to the wavelength tracking method. For larger changes of the order of 10^{-1} a parabolic fit was found to be appropriate (Fig. 5). This is due to the influence of refractive index of the medium on Fresnel reflectivities at the fiber/liquid interfaces.

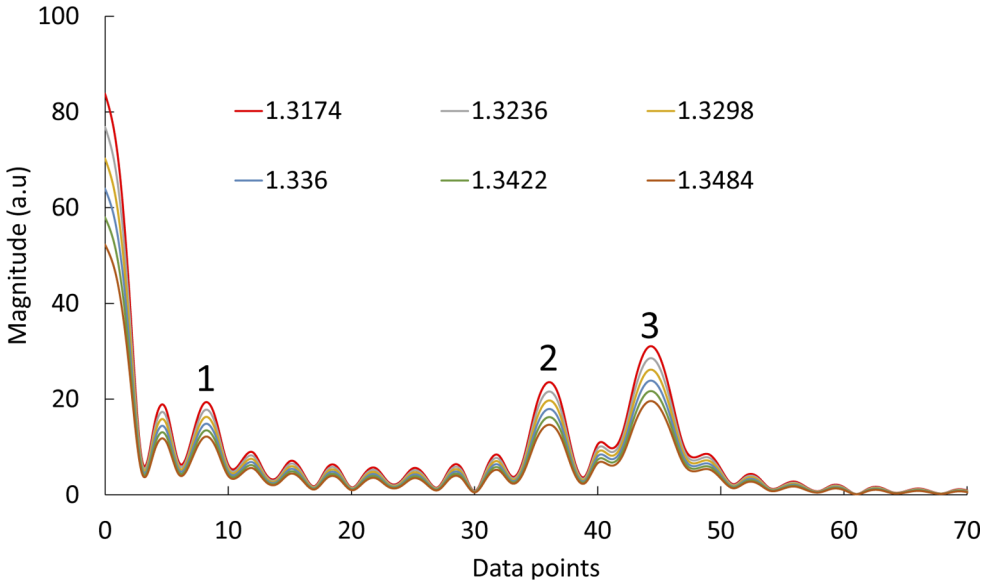

Fig. 3. FFTs of interference spectra at different refractive indices.

OSA CONTINUUM

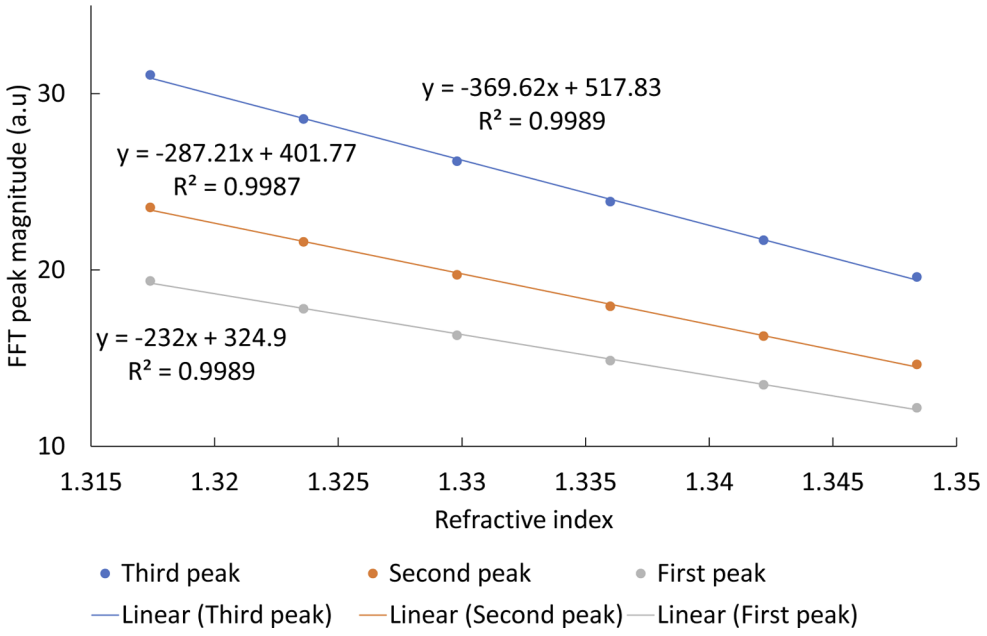

Fig. 4. Plots showing the sensitivity of FFT peak magnitudes to refractive index.

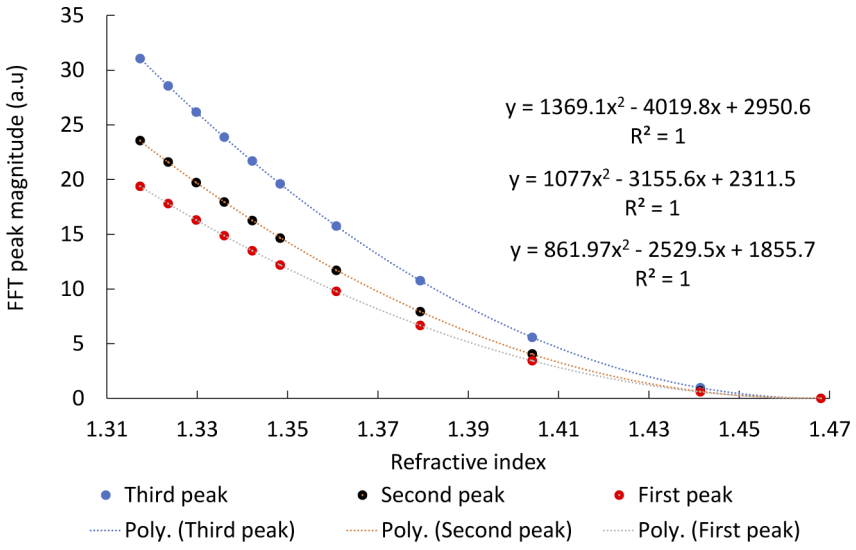

Fig. 5. Variation of FFT peak magnitudes with refractive index over a wide range.

OSA CONTINUUM

If the sensor is subjected to temperature changes such that $(\Delta\phi_{12}/\phi_{12}) << 1$, then from Eq. (4), the effect can be expressed as:

$$\frac{1}{\lambda}\frac{\Delta\lambda}{\Delta T} = \frac{\phi_1}{\phi_{12}}(\beta_m + \alpha_1) + \frac{\phi_2}{\phi_{12}}(\beta_f + \alpha_2) \tag{9}$$

β_m and β_f are the thermo-optic coefficients of the medium and fiber respectively; and α_1 and α_2 are the coefficients of thermal expansion of the cavity (d_1) and the fiber section (d_2) respectively. If $\alpha_1=\alpha_2=\alpha=0.55\times10^{-6}\ ^\circ C^{-1}$ is considered a constant and the thermo-optic of air as negligible then Eq. (6) is transformed as follows:

$$\frac{1}{\lambda}\frac{\Delta\lambda}{\Delta T} \approx \frac{\phi_2}{\phi_{12}}.\beta_f + \alpha \tag{10}$$

4. Results and discussion

4.1. Optical characterisation

Different cavities machined in SMF 28 fibers are shown in Figs. 6(a)"6(c). The edge-sharpness, debris-free and smooth topography of the near-vertical walled structures are readily apparent. The cavity shown in Fig. 6(a) was meant to produce 3-beam interference (Fig. 1), whilst the cavities shown in Figs. 6(b)–6(c) which are located several millimetres away from the shattered end of the fiber, were meant to produce 2-beam interference. In order to investigate their optical response, these cavities were illuminated using a broad-band ASE light source (Lumen Photonics, UK) and the reflected signals were monitored using an optical spectrum analyser (OSA) (MS9710B, Anritsu Ltd, UK) as described in [1]. The resulting Fabry-Perot spectral interference obtained over a wavelength range of 1470-1620 nm at a resolution of 0.07 nm and 5001 sampling points is shown in Fig. 7. The signal strength, fringe contrast and the modulation frequency are largely influenced by the following factors: (i) Ideally, the walls of the cavity across the core have to be parallel to each other in order to generate Fresnel reflections at normal incidence. In the case of Fig. 6(a), the deviation of wall-angle of the cavity walls and the fiber cleave-angle from the ideal 3-parallel-walled structure (Fig. 1) affects the Fresnel reflectivity and the back-coupling efficiency which in turn is determined by the cavity length; (ii) surface-roughness-induced scattering losses; and (iii) local variations in surface flatness or curvature also influence the fringe pattern. With reference to Fig. 6(a), the entrance and exit of the cavity are obvious. Here the entrance corresponds to opening where the micromachining was initiated on the fiber surface and exit corresponds to that which is diametrically opposite. The length of the cavity at entrance and exit were measured to be 115 µm and 102.72 µm respectively from which the wall-angle found to be ~2.8°. The calculated separation between the cavity walls at a depth of 62.5 µm was 108.83 µm. The cleaved-end of the fiber is also angled at ~3°. Stone and Marcuse [35] reported that the tilt in reflector etalon is detrimental to the peak transmission and finesse of the cavity with increasing separation between the cleaved fiber-end and the reflector etalon. The spectral interference from the circular cavity shows broadened fringes with poor contrast relative to the fringes obtained from the rectangular cavities. The visibility of the fringes obtained from a conventional extrinsic fiber Fabry-Perot sensor with similar air-gap as the circular cavity diameter was significantly higher due to the absence of curvature on the etalons. The contribution of the third reflection from the cleaved-end (Fig. 6(a)) improved the signal strength. The shattered distal ends of the fibers in Figs. 6(b)–6(c) arrest the third Fresnel reflection. The calculated air-filled cavity lengths of Figs. 6(b)–6(c) using the two-beam cavity length equation in [1] were ~62 µm and ~106 µm respectively. These lengths are reasonable with the dimensions shown in the SEM micrographs. The results demonstrate precision-control over the machining process that yields smooth topography devoid of cracks and reproducibility of Fabry-Perot microcavities. There was no obvious evidence of material redeposition at the boundary of the cavity. Interference fringes

OSA CONTINUUM

of good visibility were observed in spectral domain during optical characterisation immediately after the machining process without resorting to any post-processing methods. The production takes a typical processing time of about 20 minutes. Currently, the cavity shown in Fig. 6(a) is the subject of investigation; hence firstly we study its performance in sensing refractive index of organic solvents followed by temperature sensing.

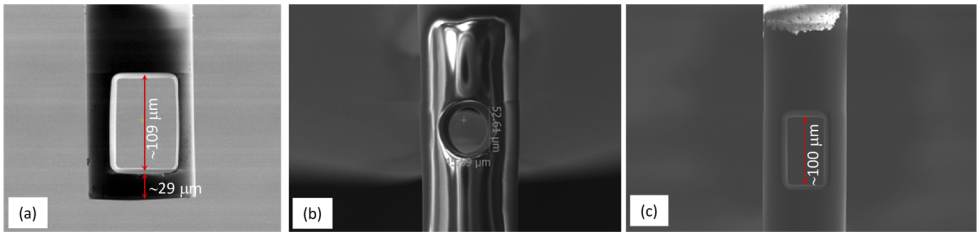

Fig. 6. (a-c) FIB-machined microcavities in SMF 28 fibers: (a) Rectangular cavity in the proximity of the cleaved-end; (b) Circular and (c) Rectangular cavities away from the shattered end of the fiber.

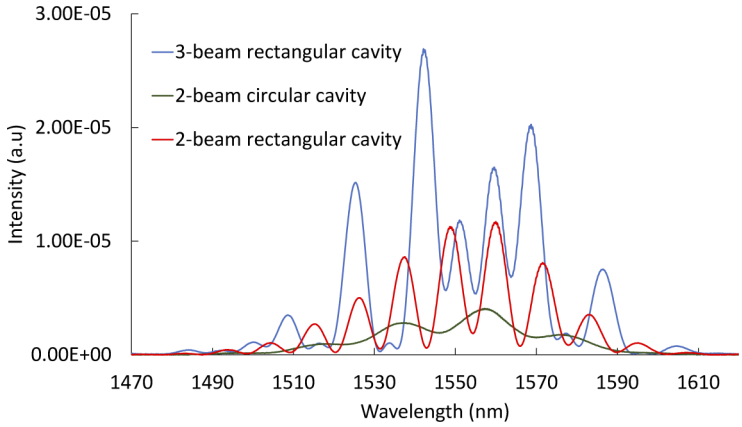

Fig. 7. Interference spectrum obtained from FIB-machined cavities in SMF 28 fibers interrogated using a broad-band light source and an OSA.

4.2. Signal processing

Signal processing was carried out on interference spectra obtained using the sweep wavelength-based interrogator during refractive index and temperature sensing unless otherwise specified. To enable accurate determination of wavelengths corresponding to the fringe maxima or minima, the high-frequency noise component present in the interference spectrum acquired using the sweep wavelength-based interrogator was smoothened using Savitzky and Golay filter. Sets of 101 consecutive data points were used to determine the best mean square fit of a cubic polynomial through the entire sweep spectrum that comprised of 19776 data points without loss of fidelity of the raw spectrum. Subsequently FFTs of the spectra were determined as described previously and then further processed using cubic spline interpolation with a sampling interval of 0.1. This was done to determine the magnitudes of FFT peaks more accurately. Figures 8(a)–8(b) shows the interference spectrum of air-filled cavity (Fig. 6(a)) at laboratory ambient conditions and its FFT. The three distinct peaks (P_1, P_2 and P_3) correspond to the spectral modulation frequencies due to the interference of Fresnel reflections (2,3; 1,2; and 1,3) respectively (Fig. 1).

OSA CONTINUUM

As mentioned previously, the relative magnitudes of these peaks can be influenced mainly by the round-trip insertion losses; imperfections in the geometry of the structure; and scattering losses. In order to estimate the OPDs, we used the method reported by Pevic and Donlagic [29] in which the interference spectrum as a function of wavelength is expressed in terms of optical frequency followed by conversion into time domain. The time-domain is shown on the secondary X-axis (Fig. 8(b)). The times corresponding to the peaks impart the respective OPDs. Prior to interpolation, the sampling time interval of 0.0412 ps corresponds to a travel distance of 8.43 µm in fiber and 12.37 µm in air. P_2 corresponds to 0.7180 ps which upon multiplication with '$v_{air}/2$'($v_{air}=3\times10^8/1.0002\ ms^{-1}$, the speed of light in air) yields $d_1=107.68$ µm, half the path difference between the reflections 1 and 2. This agrees reasonably well with the measured air-cavity length (~109 µm) in Fig. 6(a). Peak P_1 corresponds to 0.5199 ps which upon multiplication with '$v_{fiber}/2$' ($v_{fiber}=3\times10^8/1.4681\ ms^{-1}$) yields $d_2=53.12$ µm. This discrepancy with the fiber section d_2~29 µm as measured from the SEM micrograph (Fig. 6(a)) can be explained as follows:

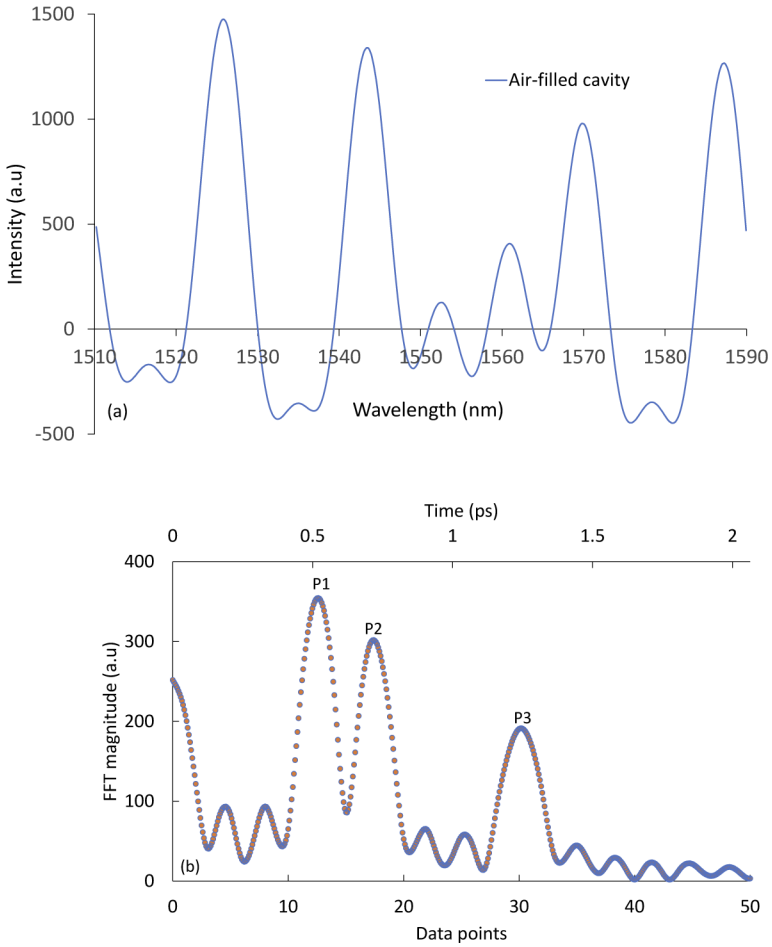

Fig. 8. (a) Interference spectrum of air-filled cavity obtained from the interrogator; and (b) the corresponding FFT.

As illustrated schematically in Fig. 9, the light coupled into the fiber section 'd_2' can experience multiple Fresnel reflections that generate path 4. The losses in between the reflections at either ends of 'd_2' can be neglected as the light is guided within the core. Assuming a normal incidence on the right-wall of the cavity and at the cleaved-end of the fiber, the reflections 3 and 4 will have

OSA CONTINUUM

a magnitude of ~93% and ~0.12% of the Fresnel reflection 2 respectively. The OPD between the reflections 2,3 and 3,4 is the same, hence should correspond to same frequency. If peak P_1 corresponds to the OPD between 2 and 4, then multiplication of $v_{fiber}/4$ with the corresponding time of 0.5199 ps yields d_2=26.56 µm which is close to the SEM-measured d_2. The contribution of such higher order reflections is generally not accounted for due to their small intensity and the resulting poor contrast of the fringes. In addition, the observed tilt at the end of the fiber section (d_2) reduces the Fresnel reflection as part of the reflected light will be lost into the cladding as the light travels backward. Despite the observed deviation from the normal cleave, as the fiber section is relatively short, the contribution of higher order reflections may have become possible. The other factor is that the sweep wavelength-based interrogators usually have a long coherence length [36] due to narrow-emission line width. Hence the intensity modulation at relatively long OPD can be observed. P_3 corresponds to a time of 1.2462 ps which is nearly equal to the sum of the times 0.7180 ps and 0.5199 ps. The difference (1.2462 ps-0.5199 ps) when multiplied by ($v_{air}/2$) yields d_1=108.94 µm. Therefore, the third peak (P_3) corresponds to the modulation frequency due to the superposition of reflections 1 and 4. The peak that infers OPD between the reflections 1 and 3 was not obvious.

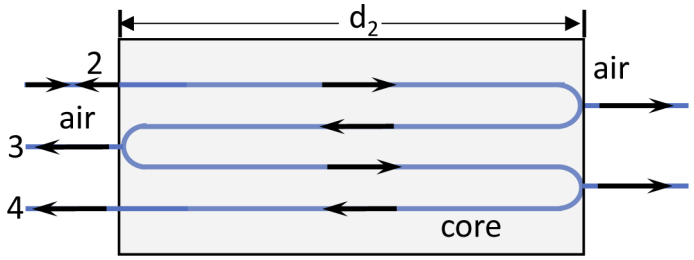

Fig. 9. Schematic illustration of the dual round-trip in the fiber section.

The observed deviation in wall-angle of the cavity can be explained as follows: The current density distribution across the focussed spot at relatively high beam currents deviates from the Gaussian profile and resembles a Holtsmark distribution characterised by a central peak with long side-tails [37,38]. As the spot is scanned across the defined pattern area as governed by the pixel spacing and dwell times along the XY-axes, the central region of the focussed ion beam excises more material as compared to the edges. The effect of this differential sputtering remains at the edges of the boundary of the defined pattern. Such an effect in conjunction with redeposition of sputtered material was reported in the case of 'Si' [39] and 'SiO_2' [40] milling. In the case of the current sensor, a pattern of 100 µm x 50 µm was defined over the curved surface of the fiber with its length parallel to the axis of the fiber. We used 1 µA milling current with 50 µs spot dwell-time and the focussed spot diameter was of the order of few micrometres as governed by the set aperture diameter. The milling was continued until a through-cavity was obtained. Given the cylindrical surface of the fiber, the angle of incidence can be expected to change over the circumference. It was reported that sputter yield for a specified material varies with the angle of incidence of the beam on the sample surface [41]. The beam would experience defocussing to some extent on the cylindrical surface of the fiber and the effects of aberrations tend to increase with increasing depth of the cavity. The influence of redeposition of the sputtered material is a major cause of wall-angle in high aspect-ratio sub-micrometre diameter cavities [40,42]. As the wall-angle in our case is only a few degrees (<3°), the effect of redeposition on the cavity walls appears to be less due to relatively large dimensions of the pattern and high beam current employed. Further quantification of redeposition requires sectioning of the cavity and analysis. The dimensions at the entrance of the cavity (~115 µm x 80 µm) post-milling exceed the set pattern dimensions (100 µm x 50 µm). The dimensional increase along the circumference

OSA CONTINUUM

was more compared to that along the length. These results may be attributed to the edge-effect in conjunction with defocussing. Fine polishing of cavity walls of FIB-milled Fabry-Perot cavities in silica fibers to improve their smoothness was reported [8,16–17]. Sputtering of redeposited material on cavity walls using relatively high beam currents was employed as a means of making the exit dimensions almost equal to those of the entrance dimensions of a through-cavity milled in silicon substrate at a low beam current [43]. In the case of our sensor, post-polishing at appropriate beam current may be employed to make the cavity walls steeper. It is also proposed that scanning along the defined line parallel to the fiber axis on the top of the cylindrical surface followed by incremental rotation to scan along the next line may aid in the mitigation of effects due to defocussing and variable angle of incidence.

The interference spectra obtained due to immersion of the sensor in different organic solvents and the corresponding FFT magnitudes are shown in Fig. 10(a-b). The refractive indices of the solvents at 1550 nm at 25 °C were taken from [44]. As the liquid infiltrates the cavity, the optical path length difference (OPD) between the Fresnel reflections 1&2 increases whilst the Fresnel return loss increases. This is apparent from the relative magnitudes of the spectral intensities of solvent-filled and air-filled cavity (Fig. 10(a) and Fig. 8(a)) and also from the FFT signals (Fig. 10(b)). The difference between the refractive indices of the solvents is large enough to induce a phase change that exceeds 2π and hence we observed a non-linear trend of fringe wavelength shift Vs refractive index. The increase in OPD due to solvent infiltration leads to an increased traverse time through the cavity. This is expected to cause a shift in P_2 and P_3 towards longer time. P_1 is expected to remain unchanged as the length of the fiber section is constant. For example, in FFT of methanol (Fig. 10(b)), P'_1 corresponds to 0.5158 ps and P_2 shifted to P'_2 that corresponds to 0.8954 ps. P'_3 corresponds to 1.4154 ps which is close to the sum of the times corresponding to P'_1 and P'_2. Hence our supposition seems reasonable.

Due to the tilt in cavity walls, the Gaussian beam experiences deflection due to refraction. The resulting lateral shift of the beam alters the coupling efficiency and also the path length as governed by the refractive index of the solvent as the light traverses the cavity length. In the absence of tilt, the change in traverse time can be attributed to the change in refractive index of the solvent only. The solvent (methanol) refractive index estimated using the time (P'_2) and the estimated d_1 (107.68 μm) of air-filled cavity was 1.2474. This discrepancy (0.07) with methanol index (1.3174) can be attributed to the change in path length due to beam shift upon solvent (methanol) infiltration. This discrepancy is significantly high compared to the thermo-optic effect on solvents, which is of the order of $\sim 10^{-4}$ °C^{-1} [45,46], due to ambient temperature variation of ±1.5 °C. As the solvent refractive index nears the core index, the beam deflection tends to cease. The intensities of P'_1 and P'_2 are relatively close to the noise floor for different solvents and hence were not considered for index calibration. For that, the magnitude of P'_3 was an obvious choice. The magnitude of the 3rd peak corresponding to different solvents was normalised with respect to that of air which acts as a reference due to the fact that its refractive index change during the duration of the experiment is negligible. A linear and parabolic fit to the data is shown in Fig. 11. The parabolic fit (Fig. 11(a)) yields a better R^2 value over a wide refractive index range as observed in theory. A linear fit to the normalised FFT peak magnitudes of solvents of Fig. 11(a) converted to dB scale ($10.\log(P_3'/P_3)$) is shown in Fig. 11(b). The refractive index sensitivity was ~-65 dB/riu. The signal amplitude resolution of the interrogator is ~0.003 dB. The estimated index resolution is $\sim 4.6 \times 10^{-5}$. However, the reason for the peak in between P'_1 and P'_2 is not obvious. This is probably due to interference between the first reflection and a part of the shifted beam reflected from the other angled-wall of the cavity. This aspect is a subject of further investigations. Given the low thermal expansion and thermo-optic coefficient of fused silica fiber, the temperature effect on the sensor due to temperature variation (25 ± 1.5 °C) can be neglected. It is obvious from these observations that the tilt in cavity walls and the cleave

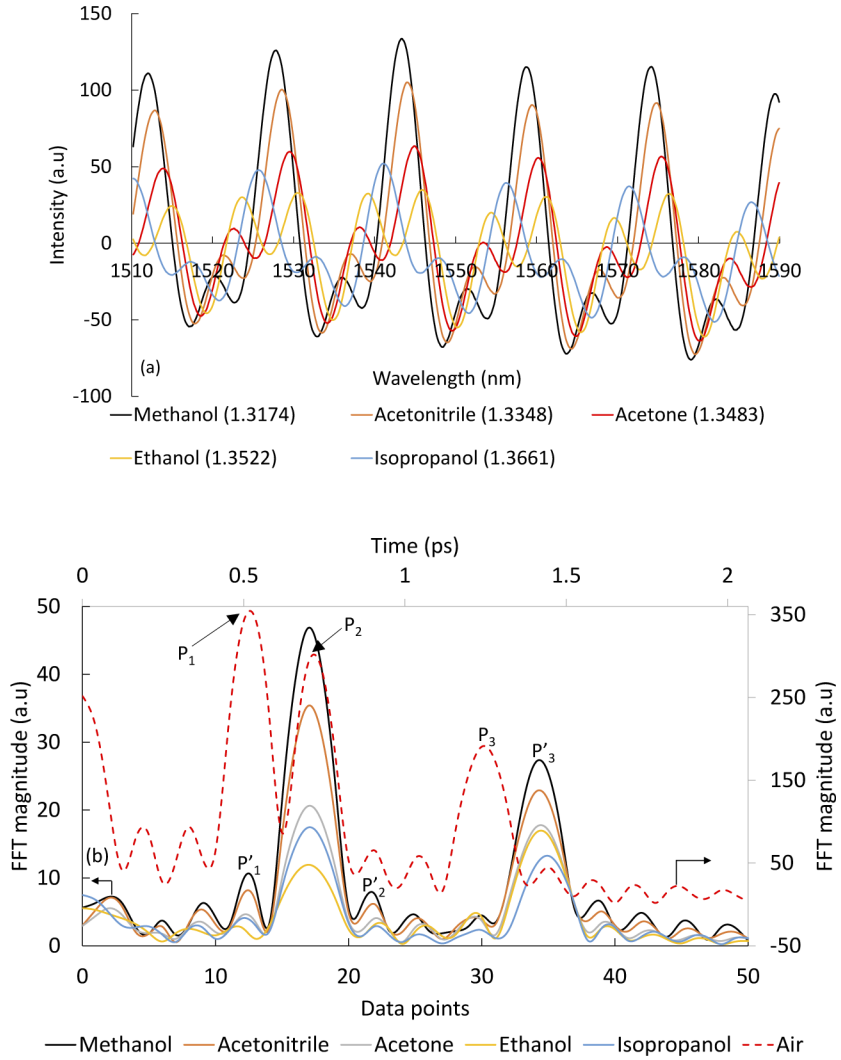

Fig. 10. (a) Interference spectra from the interrogator obtained during immersion of the sensor in different organic solvents; and (b) FFTs of the corresponding spectra.

imperfections induce errors in directly determined refractive index and that the control of these factors is essential for better accuracy and comparison with theoretical predictions.

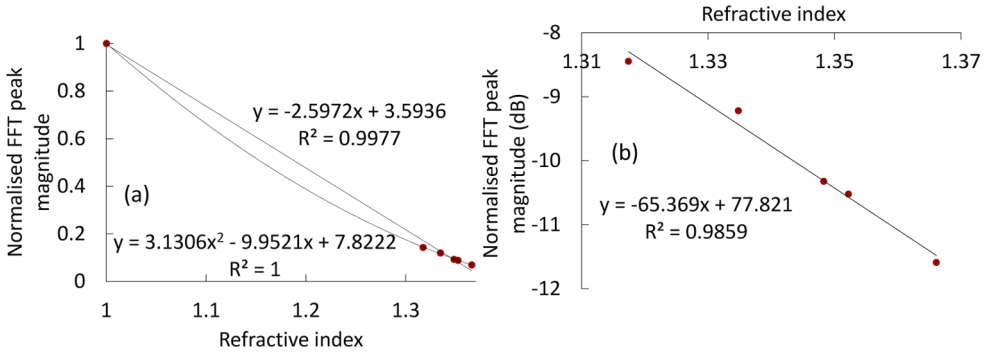

Fig. 11. Plots of 3rd peak magnitude Vs refractive index of the solvents; (a) Normalised with respect to magnitude of 3rd peak with sensor in air, (b) In dB scale over the index range of solvents.

4.3. *Temperature sensing*

Subsequent to refractive index sensing, the same sensor was used for temperature sensing. As the temperature was ramped to set isothermal temperatures, small shifts in spectral interference pattern without generation of new orders was observed. Therefore, wavelength tracking method was considered. The shift of a fringe towards longer wavelength as a result of change in the air-cavity length (d_1), fiber section (d_2) and the refractive index of the fiber is shown in Fig. 12(a). The peak wavelength of the fringe with temperature during 1st & 2nd heating is shown in Fig. 12(b). Adamovsky *et al.* [47] used Maclaurin expansion of thermo-optic and thermal expansion coefficients of silica fiber up to third order while determining their relative contributions to Bragg wavelength shift over a wide temperature range. Non-linear behaviour of thermo-optic coefficient was found to be the dominant factor whilst the thermal expansion was virtually constant. Above 770 °C, diffusion of germanium that led to grating erasure was experimentally confirmed by Energy Dispersive Spectroscopy. Our sensor response showed the best R^2-value for cubic fit (Table 1). This may be attributed to the cubic dependence of fiber index on temperature. The linear fit yields a sensitivity of 8.1 pm/°C (Table 1). The wavelength resolution of the interrogator is ~3 pm. Therefore, the estimated temperature resolution is ~0.4 °C. The broadening of index profile due to germanium diffusion can cause mode spreading into the cladding followed by beam expansion at the exit of the fiber [48]. Polyzos *et al.* [49] reported large phase drifts in Fabry-Perot sensing elements based on Ge-doped fibers as compared to pure silica fiber-based sensors at temperatures of about 1000 °C. The significantly different response of the sensor during the second heating indicates a permanent change in the non-linear thermo-optic coefficient as a result of dopant diffusion. It is required to further investigate, the influence of dopant-diffusion on the thermo-optic of Ge-doped fiber and its influence on the sensor response. A small drift in phase of the spectral interference was observed at room temperature after first heating. This sensor may be used up to temperatures below the dopant-diffusion temperature.

4.4. *Chemical sensing*

SEM micrograph of a cavity in fused silica multimode fiber and its side-view optical micrograph used for chemical sensing is shown in Figs. 13(a)–13(b). Here the cavity serves to act as a micro-spectroscopic cell. The cavity walls are tilted by ~3° from the vertical. The fiber has a low-OH pure silica core of diameter 105 μm with a numerical aperture of 0.22. Firstly, the

OSA CONTINUUM

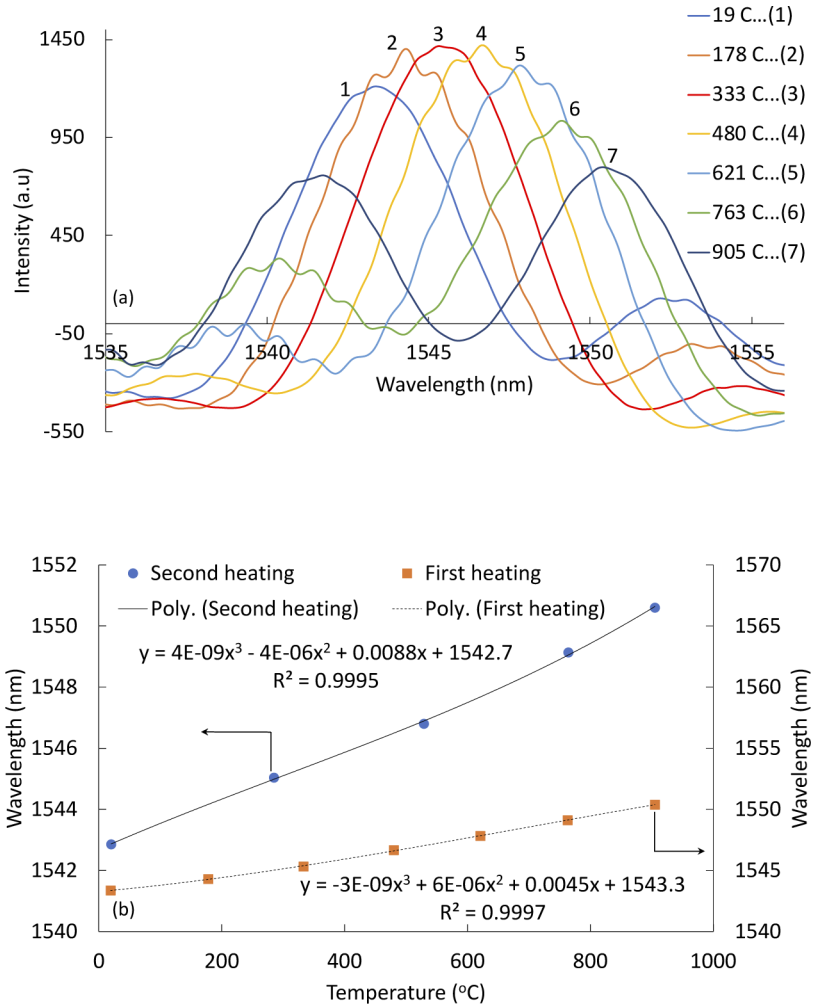

Fig. 12. (a) Shift in a fringe obtained from the interrogator with temperature during first heating; and (b) shift in peak wavelength of a fringe during first and second heating.

Table 1. Regression fits to wavelength Vs temperature data of first and second heating

Curve fit	1st heating		2nd heating	
	Equation	R^2	Equation	R^2
Linear	y = 0.0081x + 1542.9	0.9944	y = 0.0087 x + 1542.6	0.9955
Quadratic	y = 2E-06x² + 0.006x + 1543.2	0.9992	y = 2E-06x² + 0.0068 x + 1542.8	0.9988
Cubic	y = -3E-09x³ + 6e-06x² + 0.0045x + 1543.3	0.9997	y = 4E-09x³ - 4e-06x² + 0.0088x + 1542.7	0.9995

OSA CONTINUUM

sensor was used to obtain the absorption spectrum of amine-based hardener. Then the sensor was cleaned with acetone and allowed to dry. The air-filled cavity signal was retrieved after cleaning. Subsequently, epoxy resin was studied. The absorption spectra of the amine-based hardener and the epoxy obtained using this sensor at an average of 128 scans and a resolution of 4 cm^{-1} are shown in Fig. 14. Although some degree of cavity wall-angle was obvious, the coupling efficiency through the resin-filled cavity was found to be adequate to obtain absorbance spectra with clearly discernible peaks. Assignment of different peaks to the respective functional groups [50,51] is presented in Table 2. Amine-based hardener has affinity for atmospheric moisture. As the infiltrated amine was exposed to laboratory ambient for 15 hours, the absorbed moisture was obvious via the OH-peak (Fig. 15). This offers scope for the detection of moisture ingress and cross-linking reactions of thermosetting resins used in the production of aerospace composites.

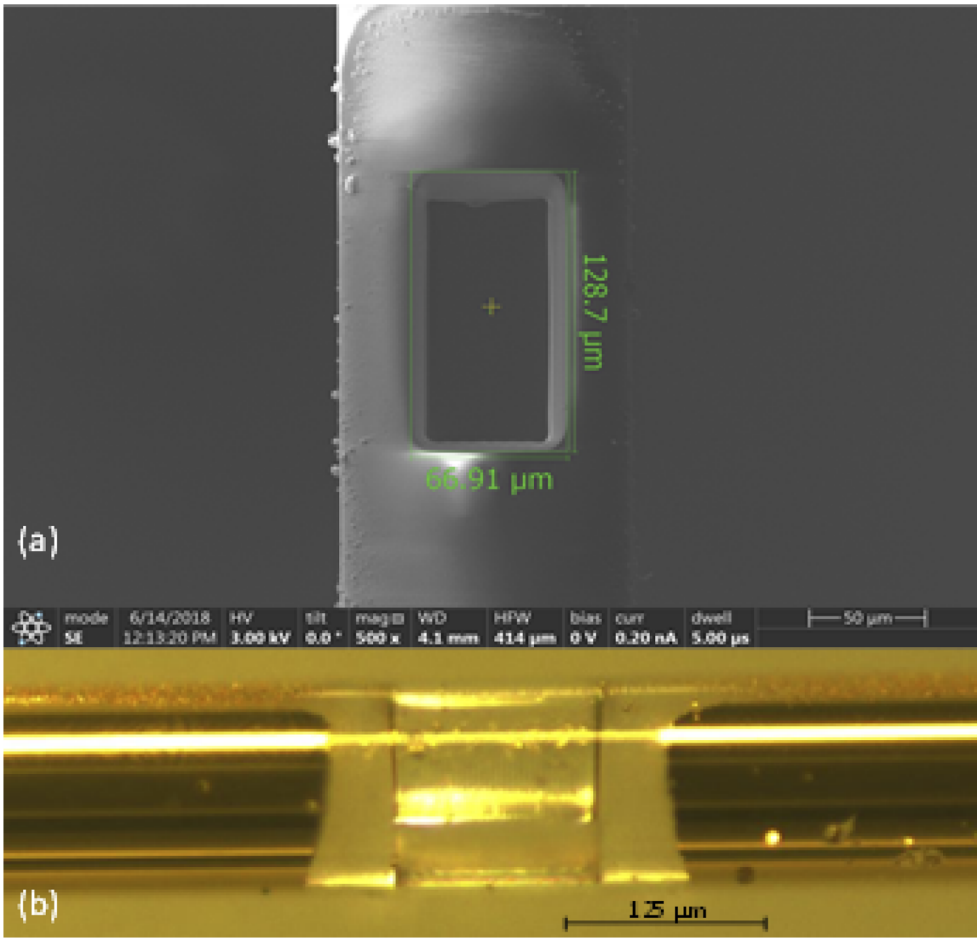

Fig. 13. (a) SEM micrograph of a cavity in fused silica multimode fiber and (b) optical micrograph of the side-view of the same cavity.

OSA CONTINUUM

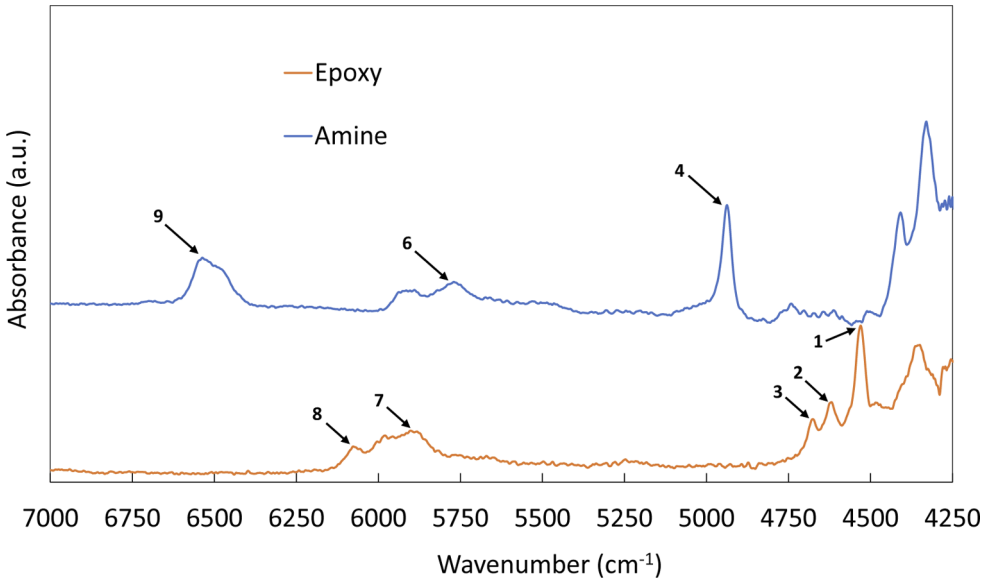

Fig. 14. Absorbance spectra of epoxy and amine-based hardener obtained using the fiber sensor.

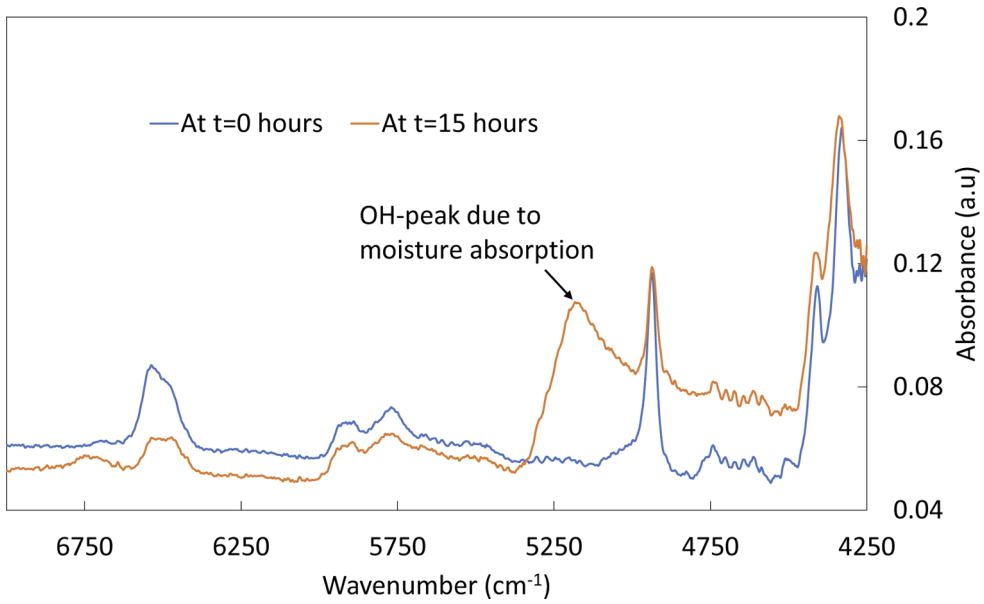

Fig. 15. Absorbance spectra of amine-based hardener before and after exposure to laboratory ambient.

OSA CONTINUUM

Table 2. Assignment of absorption peak wavelengths to different functional groups.

Peaks	Wavenumber (cm^{-1})	Functional Group Assignment
1	4530.9	C-H stretching (epoxy)
2,3	4619.7,4667.9	C-H stretching (aromatic combination band)
4	4936.1	N-H stretching and bending (primary amine combination band)
5	5236.9	O-H asymmetric stretching and bending (due to moisture)
6	5767.4	Aliphatic, terminal R-CH_3 overtone (stretching)
7	5890.3	Combination of epoxy and primary amine overtones
8	6068.2	C-H stretching (terminal epoxy overtone)
9	6533.1	Primary and secondary amine combination band

5. Summary and conclusions

Xenon plasma FIB-based micromachining of fused silica optical fibers for controlled production of Fabry-Perot cavities in single mode fibers was demonstrated. The sensor production was relatively rapid without any post-processing. Theoretically, the magnitudes of FFT peaks corresponding to the superposition of 3-normal Fresnel reflections produced from a Fabry-Perot cavity micromachined in the proximity of the cleaved-end of a fiber show different sensitivities to refractive index of infiltrated liquid. Larger cavity length yields a higher refractive index sensitivity but at the expense of the refractive index range. The micromachined rectangular cavities generating 2 and 3-beam spectral interference was characterised by good contrast fringes whilst the circular cavity showed significant loss of fringe contrast. A single-ended 3-beam-based FP cavity was investigated for refractive index and temperature sensing. The estimation of lengths of air-filled cavity and the fiber-section by means of FFT-based round-trip traverse time calculations was reasonably accurate. Evidence of interference of higher order Fresnel reflections due to the short length of the fiber section was observed. The deviation of the cavity wall-angle and the fiber cleave angle from the ideal 3-parallel-walled geometry has induced errors in the measured refractive indices. This is due to the refraction of the Gaussian beam at the tilted walls of the cavity that alters the beam path and also the coupling efficiency as governed by the refractive index of the solvent. Therefore, the change in optical path is due not only to the solvent refractive index but also to the beam path. Despite the observed deviations, the magnitude of the third FFT peak Vs the refractive index showed an excellent linearity offering a scope for use as a pre-calibrated sensor. Therefore, the control of cavity wall-angle is key to the direct and accurate measurement of refractive index via this single-ended sensor design. FIB-polishing of the cavity walls post-machining or FIB-machining via the proposed scan and rotate technique may be employed to further control the tilt-angle of cavity walls.

The response of the same sensor to temperature up to 900 °C concurs with the non-linear response of the thermo-optic coefficient of the Ge-doped fiber. This single-ended sensor design can be isolated from strain by sealing it inside a silica capillary for temperature sensing up to the onset of dopant diffusion. Further investigations are underway to determine the influence of dopant diffusion on the thermo-optic of the fiber over a wide temperature range.

A rectangular cavity in the multimode fiber served as a micro-spectroscopic cell. It enabled absorption spectroscopy of a thermoset resin and amine-based hardener which form primary constituents of a thermoset resin system. The absorption of moisture by amine-based hardener was also detected. With a cavity in multimode fiber micromachined in the proximity of a mirror-coated cleaved-end of a multimode fiber, reflection spectroscopy via a single ended design

OSA CONTINUUM

could be enabled. Potential applications include remote multipoint cure monitoring in complex shaped composite structures; moisture and chemical ingress; gas sensing and biological sensing.

Funding. Defence Science and Technology Laboratory Grant (DSTLX-1000133262R), UK.

Acknowledgments. IK acknowledges funding from the Engineering and Physical Sciences Research Council for a PhD studentship. The authors are grateful for the technical assistance given by Paul Stanley (UoB). The authors also wish to acknowledge the practical support given by Frank Biddlestone. VRM would like to thank Prof. M Sreenivasarao for stimulating discussions and Bongkot Hararak for her assistance. VRM and GFF dedicate this work as a sincere tribute to the Late Prof. Brian Ralph, former President of the Royal Microscopical Society, UK for being a mentor, philosopher and a compassionate academic who helped and inspired us all the way through our careers.

Disclosures. The authors declare that there are no conflicts of interest related to this article.

References

1. V. R. Machavaram, R. A. Badcock, and G. F. Fernando, "Fabrication of intrinsic fiber Fabry–Perot cavities in silica optical fibers via F_2 -laser ablation," Meas. Sci. Technol. **18**(3), 928–934 (2007).
2. Y. J. Rao, Z. L. Ran, X. Liao, and H. Y. Deng, ", "Hybrid LPFG/MEFPI sensor for simultaneous measurement of high-temperature and strain," Opt. Express **15**(22), 14936–14941 (2007).
3. Y. J. Rao, M. Deng, D. W. Duan, X. C. Yang, T. Zhu, and G. H. Cheng, "Micro Fabry-Perot interferometers in silica fibers machined by femtosecond laser," Opt. Express **15**(21), 14123–14128 (2007).
4. T. Wei, Y. Han, H. L. Tsai, and H. Xiao, "Miniaturized fiber inline Fabry–Perot interferometer fabricated with a femtosecond laser," Opt. Lett. **33**(6), 536–538 (2008).
5. V. R. Machavaram, R. A. Badcock, and G. F. Fernando, "Fabrication of intrinsic fiber Fabry–Perot sensors in silica fibers using hydrofluoric acid etching," Sens. Actuators, A **138**(1), 248–260 (2007).
6. Y. Zhang, X. Chen, Y. Wang, K. L. Cooper, and A. Wang, "Microgap multicavity Fabry–Pérot biosensor," J. Lightwave Technol. **25**, 1797–1804 (2007).
7. P. A. R. Tafulo, P. A. S. Jorge, J. L. Santos, F. M. Araujo, and O. Frazao, "Intrinsic Fabry–Pérot Cavity Sensor based on etched multimode graded index fiber for strain and temperature measurement," IEEE Sens. J. **12**(1), 8–12 (2012).
8. R. M. André, S. C. Warren-Smith, M. Becker, J. Dellith, M. Rothhardt, M. I. Zibaii, H. Latifi, M. B. Marques, H. Bartelt, and O. Frazão, "Simultaneous measurement of temperature and refractive index using focused ion beam milled Fabry-Perot cavities in optical fiber micro-tips," Opt. Express **24**(13), 14053–14065 (2016).
9. J. I. Kou, J. Feng, L. Ye, F. Xu, and Y. Q. Lu, "Miniaturized fiber taper reflective interferometer for high temperature measurement," Opt. Express **18**(13), 14245–14250 (2010).
10. S. Krishnamurthy, R. A. Badcock, V. R. Machavaram, and G. F. Fernando, "Monitoring pre-stressed composites using optical fiber sensors," Sensors **16**(6), 777 (2016).
11. S. Karimelahi, L. Abolghasemi, and P. R. Herman, "Rapid micromachining of high aspect ratio holes in fused silica glass by high repetition rate picosecond laser," Appl. Phys. A: Mater. Sci. Process. **114**(1), 91–111 (2014).
12. V. R. Machavaram, R. A. Badcock, and G. F. Fernando, "F_2-laser ablation of Fabry–Perot cavities in optical fibers: chemical sensors," J. Opt. A: Pure Appl. Opt. **14**(3), 035602 (2012).
13. S. Kiyama, S. Matsuo, S. Hashimoto, and Y. Morihira, "Examination of etching agent and etching mechanism on femto-second laser microfabrication of channels inside vitreous silica substrates," J. Phys. Chem. C **113**(27), 11560–11566 (2009).
14. I. A. Konovalov and P. R. Herman, "Ablation-induced stresses in fused silica by 157-nm F2-laser irradiation," Mater. Res. Soc. Symp. Proc. **617**, J3.3 (2000).
15. Y. Bellouard, "On the bending strength of fused silica flexures fabricated by ultrafast lasers," Opt. Express **1**(5), 816–831 (2011).
16. J. Li, F. Albri, R. R. J. Maier, W. Shu, J. Sun, D. P. Hand, and W. N. MacPherson, "A micro-machined optical fiber cantilever as a miniaturized pH sensor," IEEE Sens. J. **15**(12), 7221–7228 (2015).
17. J. Sun, J. Li, R. R. J. Maier, D. P. Hand, W. N. MacPherson, M. K. Miller, J. M. Ritchie, and X. Luo, "Fabrication of a side aligned optical fiber interferometer by focused ion beam machining," J. Micromech. Microeng. **23**(10), 105005 (2013).
18. X. Li, Y. Shao, Y. Yu, Y. Zhang, and S. Wei, "A highly sensitive fiber-optic Fabry-Perot interferometer based on internal reflection mirrors for refractive index measurement," Sensors **16**(24), C1 (2016).
19. L. V. Nguyen, M. Vasiliev, and K. Alameh, "Three-wave fiber Fabry-Perot interferometer for simultaneous measurement of temperature and salinity of seawater," IEEE Photo. Tech. Lett. **23**(7), 450–452 (2011).
20. J. Sirkis, T. A. Berkoff, R. T. Jones, H. Singh, A. D. Kersey, E. J. Friebele, and M. A. Putnam, "In-line fiber etalon (ILFE) fiber-optic strain sensors," J. Lightwave Technol. **13**(7), 1256–1263 (1995).
21. F. Shen and A. Wang, "Frequency-estimation-based signal-processing algorithm for white-light optical fiber Fabry–Perot interferometers," Appl. Opt. **44**(25), 5206–5214 (2005).
22. M. Deng, C. P. Tang, T. Zhu, Y. J. Rao, L. C. Xu, and M. Han, "Refractive index measurement using photonic crystal fiber-based Fabry–Perot interferometer," Appl. Opt. **49**(9), 1593–1598 (2010).

OSA CONTINUUM

23. L. Yan, Z. Gui, G. Wang, Y. An, J. Gu, M. Zhang, X. Liu, Z. Wang, G. Wang, and P. Jia, "A micro bubble structure based Fabry–Perot optical fiber strain sensor with high sensitivity and low-cost characteristics," Sensors **17**(3), 555 (2017).
24. C. L. Lee, C. H. Hung, C. M. Li, and Y. W. You, "Simple air-gap fiber Fabry–Perot interferometers based on a fiber endface with Sn-microsphere overlay," Opt. Commun. **285**(21-22), 4395–4399 (2012).
25. T. Wei, Y. Han, Y. Li, H. L. Tsai, and H. Xiao, "Temperature-insensitive miniaturized fiber inline Fabry-Perot interferometer for highly sensitive refractive index measurement," Opt. Express **16**(8), 5764–5769 (2008).
26. Y. Zhang, L. Yuan, X. Lan, A. Kaur, J. Huang, and H. Xiao, "High-temperature fiber-optic Fabry–Perot interferometric pressure sensor fabricated by femtosecond laser," Opt. Express **39**(1), 4609–4612 (2014).
27. Z. L. Ran, Y. J. Rao, W. J. Liu, X. Liao, and K. S. Chiang, "Laser-micromachined Fabry-Perot optical fiber tip sensor for high-resolution temperature-independent measurement of refractive index," Opt. Express **16**(3), 2252–2263 (2008).
28. H. Y. Choi, G. Mudhana, K. S. Park, U.-C. Paek, and B. H. Lee, "Cross-talk free and ultra-compact fiber optic sensor for simultaneous measurement of temperature and refractive index," Opt. Express **18**(1), 141–149 (2010).
29. S. Pevec and D. Donlagic, "High resolution, all-fiber, micro-machined sensor for simultaneous measurement of refractive index and temperature," Opt. Express **22**(13), 16241–16253 (2014).
30. T. L. Burnett, R. Kelly, B. Winiarski, L. Contreras, M. Daly, A. Gholinia, M. G. Burke, and P. J. Withers, "Large volume serial section tomography by Xe Plasma FIB dual beam microscopy," Ultramicroscopy **161**, 119–129 (2016).
31. J. Liu, R. Niu, J. Gu, M. Cabral, M. Song, and X. Liao, "Effect of ion irradiation introduced by focussed ion-beam milling on the mechanical behaviour of sub-micron sized samples," Sci. Rep. **10**(1), 1–8 (2020).
32. X. Zhong, C. A. Wade, P. J. Withers, X. Zhou, C. Cai, S. J. Haigh, and M. G. Burke, "Comparing Xe^+ Pfib and Ga^+ FIB for TEM sample preparation of Al alloys: Minimising FIB-induced artefacts," *J. Microsc. (Oxford, U. K.)* jmi.12983 (2020).
33. J. E. Halpin, R. W. H. Webster, H. Gardner, M. P. Moody, P. A. J. Bagot, and D. A. MacLaren, "An in-situ approach for preparing atom probe tomography specimens by xenon plasma-focussed ion beam," Ultramicroscopy **202**, 121–127 (2019).
34. H. Kogelnik, "Coupling and conversion coefficients for optical modes," Proc. Symposium on Quasi-optics 14, 333–347 (1964).
35. J. Stone and D. Marcuse, "Ultrahigh finesse fiber Fabry–Perot interferometers," J. Lightwave Technol. **4**(4), 382–385 (1986).
36. E. Chehura, S. W. James, S. Staines, C. Groenendijk, D. Cartie, S. Portet, M. Hugon, and R. P. Tatam, "Production process monitoring and post-production strain on a full-scale carbon fiber composite aircraft tail cone assembly using embedded optical fiber sensors," Meas. Sci. Technol. **31**(10), 105204 (2020).
37. N. I. Borgardt and A. V. Rumyantsev, "Prediction of surface topography due to finite pixel spacing in FIB milling of rectangular boxes and trenches," J. Vac. Sci. Technol. **34**(6), 061803 (2016).
38. N. S. Smith, W. P. Skoczylas, S. M. Kellogg, D. E. Kinion, P. P. Tesch, O. Sutherland, A. Aanesland, and R. W. Boswell, "High brightness inductively coupled plasma source for high current focused ion beam applications," J. Vac. Sci. Technol., B: Microelectron. Nanometer Struct.–Process., Meas., Phenom. **24**(6), 2902–2906 (2006).
39. W. C. L. Hopman, F. Ay, W. Hu, V. J. Gadgil, L. Kuipers, M. Pollnau, and R. M. D. Ridder, "Focused ion beam scan routine, dwell time and dose optimizations for submicrometre period planar photonic crystal components and stamps in silicon," Nanotechnology **18**(19), 195305 (2007).
40. S. Tan, R. Livengood, Y. Greenzweig, Y. Drezner, and D. Shima, "Probe current distribution characterization technique for focused ion beam," J. Vac. Sci. Technol. **30**(6), 06F606 (2012).
41. J. Vasile, Z. Niu, R. Nassar, W. Zhang, and S. Liu, "Focused ion beam milling: Depth control for three-dimensional microfabrication," J. Vac. Sci. Technol., B: Microelectron. Process. Phenom. **15**(6), 2350–2354 (1997).
42. J. H. Kim, J. H. Boo, and Y. J. Kim, "Effect of stage control parameters on FIB milling process," Thin Solid Films **516**(19), 6710–6714 (2008).
43. A. V. Stanishevsky, "Focused ion beam nanofabrication," in *Encyclopaedia of Nanoscience and Nanotechnology*, H. S. Nalwa, ed. (American Scientific, 2004).
44. J. E. Saunders, C. Sanders, H. Chen, and H. P. Loock, "Refractive indices of common solvents and solutions at 1550 nm," Appl. Opt. **55**(4), 947–953 (2016).
45. Y. H. Kim, S. J. Park, S. W. Jeon, S. Ju, C. S. Park, W. T. Han, and B. H. Lee, "Thermo-optic coefficient measurement of liquids based on simultaneous temperature and refractive index sensing capability of a two-mode fiber interferometric probe," Opt. Express **20**(21), 23744–23754 (2012).
46. K. Moutzouris, M. Papamichael, S. C. Betsis, I. Stavrakas, G. Hloupis, and D. Triantis, "Refractive, dispersive and thermo-optic propertiesof twelve organic solvents in the visible and near-infrared," Appl. Phys. B: Lasers Opt. **116**(3), 617–622 (2014).
47. G. Adamovsky, S. F. Lyuksyutov, J. R. Mackey, B. M. Floyd, U. Abeywickrema, I. Fedin, and M. Rackaitis, "Peculiarities of thermo-optic coefficient under different temperature regimes in optical fibers containing fiber Bragg gratings," Opt. Commun. **285**(5), 766–773 (2012).
48. K. Shiraishi, Y. Aizawa, and S. Kawakami, "Beam expanding fiber using thermal diffusion of the dopant," J. Lightwave Technol. **8**(8), 1151–1161 (1990).

OSA CONTINUUM

49. D. Polyzos, J. Mathew, W. N. MacPherson, and R. R. J. Maier, "Effect of dopant diffusion on the long-term stability of Fabry–Perot optical fiber sensors," J. Lightwave Technol. **35**(24), 5317–5323 (2017).
50. A. K. Nair, V. R. Machavaram, R. S. Mahendran, S. D. Pandita, C. Paget, C. Barrow, and G. F. Fernando, "Process monitoring of fiber reinforced composites using a multi-measurand fiber-optic sensor," Sens. Actuators, B **212**, 93–106 (2015).
51. R. S. Mahendran, L. Wang, V. R. Machavaram, S. D. Pandita, R. Chen, S. N. Kukureka, and G. F. Fernando, "Fiber-optic sensor design for chemical process and environmental monitoring," Optics and Lasers in Engineering **47**(10), 1069–1076 (2009).